Assessing the Quality of the Radiometric and Spectral Calibration of *casi* Data and Retrieval of Surface Reflectance Factors

Anne Jacobsen, Kathleen B. Heidebrecht, and Alexander F.H. Goetz

Abstract

The spectral and radiometric data quality of the Compact Airborne Spectrographic Imager (casi) was assessed using atmospheric modeling and fitting the band center location of the oxygen absorption feature centered around 0.762 μm. Atmospheric modeling was used to assess the quality of the radiometric calibration. A software program that locates the position of the oxygen absorption feature and performs atmospheric modeling was used to assess the spectral calibration of the scanner. These methods were adequate to reveal problems with the radiometric and spectral calibration and spectral alignment. The analyses required image data with a continuous spectrum and were performed on spectral mode data.

Based on one calibration target, two different methods for retrieving surface reflectance factors were applied to the spectral and spatial mode data, respectively. Atmospheric modeling and normalization to the calibration target were used on the spectral image data because water vapor correction on a pixel-by-pixel basis was possible. Water vapor correction on a pixel-by-pixel basis was not possible on the spatial data, and surface reflectance retrieval was accomplished using modeled path radiance and field spectra from the calibration target.

Introduction

The quality of image data from a commercial scanner such as the Compact Airborne Spectrographic Imager (*casi*) may vary depending on the maintenance of the scanner. For every instrument the user must assess the quality of the calibration. The calibration data provided by the operator may not always be reliable; in the worst cases, small companies may go out of business and the remote sensing analyst is left with little additional post-flight information. Particularly in these cases it becomes important to be resourceful in assessing the quality of the radiometric and spectral calibration of the data.

A. Jacobsen is with the National Environmental Research Institute, Department of Landscape Ecology, Grenåvej 14, DK-8410 Rønde, Denmark and the Institute of Geography, University of Copenhagen, Øster Voldgade 10, DK-1350 Copenhagen K, Denmark.

K.B. Heidebrecht is with the Center for the Study of Earth from Space (CSES)/CIRES, University of Colorado at Boulder, Boulder, CO 80309.

A.F.H. Goetz is with the Center for the Study of Earth from Space (CSES)/CIRES and the Department of Geological Sciences, University of Colorado at Boulder, Boulder, CO 80309.

The spectral range and resolution of the *casi* varies with the mode of operation. The spectral mode provides high spectral resolution, collecting a continuous spectrum. In contrast, the spatial mode utilizes discrete spectral intervals. The character of the two modes is important and should be considered before any calibration method, including surface reflectance retrieval, is applied to the data.

In summer 1997, a Canadian company was contracted to do a commercial flight as part of the DANish Multisensor Airborne Campaign (DANMAC). DANMAC is a multi-sensor and multi-disciplinary remote sensing program with the aim to increase the understanding of surface processes at solar and radar wavelengths. The campaign covered four different applications, including agriculture, landscape ecology, inland waters, and forestry. The *casi* flight contributed to the campaign with optical airborne data in the spectral range from 0.4 to 0.9 μm. Because the hyperspectral scanner was flown in a multi-purpose campaign, *casi* was a good choice because of the capability for user-defined spatial and spectral configurations. The application of these data presented in our study was related to landscape ecology with special emphasis on encroachment of scrubs on dry grasslands and grassland quality.

Image Data

The *casi* is a pushbroom imaging spectrograph that operates in the visible and near-infrared (VNIR) from 0.4 to 0.9 μm. The *casi* may be programmed in three different modes: spatial, spectral, and full frame. Our study used two *casi* images in spatial and spectral mode, respectively. In the spatial mode, one may obtain up to 19 spectral bands at full resolution across-track of 512 pixels. In the spectral mode, one may obtain up to 288 spectral bands at 1.8 nm in up to 512 adjacent pixels. The spectral resolution measured as the full spectral width at half maximum (FWHM) was 2.2 nm at 0.650 μm. In addition to the spectral radiance, the *casi* scanner has the option of recording the incoming light with an incident light sensor (ILS) on the roof of the aircraft that may be configured similar to the scanner. The *casi* scanner in question had a 42° field of view (FOV) but a discrepancy in the left-most 5°.

For the study of encroachment of scrubs, a high spatial resolution was required, and a 2- by 2-m ground resolution at

Photogrammetric Engineering & Remote Sensing
Vol. 66, No. 9, September 2000, pp. 1083–1091.

0099-1112/00/6609–1083$3.00/0

TABLE 1. DATA FOR THE SPECTRAL AND SPATIAL MODE OF THE *casi* USED IN THE STUDY. RSF = ROW SUMMATION FACTOR. PS = PIXEL SPACING

Date of Acquisition	10 June 1997
Location	Denmark, Jutland
Center Point	
spectral mode	56°12′48″N, 10°32′15″E
spatial mode	56°12′49″N, 10°32′04″E
Time of Acquisition	
spectral mode	13:25 local summer time
spatial mode	13:08 local summer time
Local Solar Time	
spectral mode	12:05
spatial mode	11:47
Scan Time	
spectral mode	72 seconds
spatial mode	75 seconds
Integration Time	
spectral mode	55 mseconds
spatial mode	38 mseconds
Spatial Resolution	
spectral mode	(2m by 2.8m)
spatial mode	(2m by 2m)
Spectral Range	
spectral mode	0.4 to 0.9 μm
spatial mode	0.4 to 0.8 μm
Spectral Configuration	
spectral mode	96 continuos bands, RSF 3, PS 8
spatial mode	11 discrete bands (Table 2)
Heading	
spectral mode	1°N
spatial mode	1°N
Visibility	30 to 35 km
Atmospheric Model	Continental
Altitude	1326 m

TABLE 2. KGRAS: ELEVEN-BAND SPECTRAL CONFIGURATION OF THE SPATIAL *casi* IMAGE USED IN THE STUDY. WAVELENGTHS ARE IN μM OF CENTER OF MIN AND MAX ROWS. FWHM VALUES OF EACH BAND ARE CALCULATED AS FOLLOWS: FWHM MIN = BAND MIN −1.1 NM. FWHM MAX = BAND MAX + 1.1 NM.

Band	Min (μm)	Max (μm)	FWHM (nm)	Center Wavelength (μm)
1	Frame smear			
2	0.417	0.431	16.3	0.424
3	0.470	0.480	12.8	0.475
4	0.519	0.530	12.8	0.525
5	0.544	0.555	12.9	0.550
6	0.596	0.606	12.8	0.601
7	0.646	0.655	11.1	0.650
8	0.678	0.687	11.1	0.682
9	0.710	0.719	11.2	0.715
10	0.732	0.741	11.2	0.736
11	0.764	0.773	11.2	0.769
12	0.797	0.806	11.2	0.801

nadir was achieved from a flying altitude of 1326 m. In the spectral mode, 96 bands with a spectral sampling of 5.4 nm were recorded for every ninth pixel across track. Because of the spectral priorities, the integration time was 55 ms and the resulting spatial resolution along track was 2.8 m. In spatial mode, the match of the integration time of the scanner with the speed of the aircraft was good. An 11-band configuration had an integration time of 38 ms, and a 2-m resolution along track was obtained. Both images were acquired flying almost due north and close to solar noon in order to diminish bi-directional reflectance effects. The acquisition parameters of the spatial and spectral mode data are listed in Tables 1 and 2.

Figure 1. Subset of the *casi* spectral and spatial dataset used in the study. In the spatial dataset (right) light grassland, dark forest, and white gravel roads are easily seen. The surface cover is also recognizable in the spectral image (left). The spectral image was acquired with 39 look angles and pixel spacing 8. Nadir was erroneously shifted to the left on the spectral image. Spatial image shows band 8, 0.682 μm; spectral image shows band 56, 0.687 μm.

The bandset configuration (KGRAS) in spatial mode was based on the knowledge of the variation of a typical vegetation spectrum, preliminary studies of separabilities of spectral signatures of Danish grasslands (Jacobsen *et al.*, 1995), and a bandset (GEOBOTS) that was used by other investigators for forestry inventory using *casi* data (Baulies and Pons, 1995).

The image (Figure 1) covers a softly undulated moraine landscape with grasslands at different succession stages (light areas with scrubs as dark spots), and coniferous and deciduous forests and plantations (dark areas). Gravel roads (white lines) transect the whole area. The land cover is easily recognizable on the spatial image and the structure can also be seen in the spectral raked image.

The operating company supplied image files of spectral radiance, but little information on the spectral configuration, radiance units, and scaling factors. Information about the spectral configuration in spatial mode was contradictory, and no information about the spectral mode configuration was provided. The spatial mode configuration listed in Table 2 was one of three possibilities.

We compared a *casi* radiance profile with an Airborne Visible/Infrared Imaging Spectrometer (AVIRIS) (Vane *et al.*, 1993) radiance profile acquired at approximately the same latitude and the same time of the year (Figure 2). The scaling factor of the AVIRIS data in question was 500 μW/cm^2/sr/nm. Scaling the *casi* radiance by a factor of 2 (Figure 2) indicated that *casi* scaling was 1000 μW/cm^2/sr/nm. Notice that, at the AVIRIS altitude of 20 km, there is a strong influence from path radiance in the shorter wavelengths.

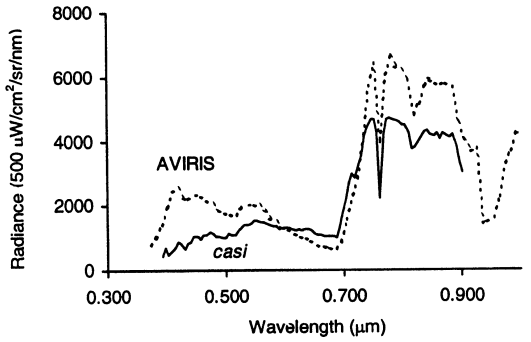

Figure 2. Radiance profile from AVIRIS (dotted) and *casi* (solid) data scaled to 500 $\mu W/cm^2/sr/nm$. AVIRIS radiance profile is from an alfalfa field in Harvard Forest, Massachusetts. Difference in radiance is seen around 0.55 μm (the green peak), around 0.67 μm (the chlorophyll absorption feature), and in the near IR region. This is due to difference in vegetation cover. Difference in radiance in the scattering part of the spectrum is due in part to different platform altitudes.

Methods

Our approach to evaluate a *casi* image data set with respect to radiometric and spectral calibration was primarily based on radiative transfer modeling and the location of the oxygen absorption feature centered around 0.762 μm. The methods were applicable to the spectral mode data because these data were recorded as continuous spectra.

Atmospheric Modeling

Scattering and absorption by dry air molecules and particulate matter attenuate the transmission of solar radiation through the atmosphere. The scattering component of the continuum attenuation is the path radiance, which is the amount of radiation that is reflected from the atmosphere to the scanner without any interaction with the ground. Scattering of dry air molecules (Rayleigh scattering) decreases rapidly with wavelength ($\sim\lambda^{-4}$) whereas scattering of particulate matter decreases less rapidly (Iqbal, 1983). Generally speaking, 10 percent of the radiation measured at a satellite at 1.0 μm is made up of scattered light (Gao *et al.*, 1993).

Absorption of solar radiation by gases (dry air molecules and water vapor) is a selective process that occurs only at discrete wavelengths (Iqbal, 1983). The main molecular absorbers in the atmosphere are water vapor (H_2O), carbon dioxide (CO_2), ozone (O_3), nitrous oxide (N_2O), carbon monoxide (CO), oxygen (O_2), methane (CH_4), and nitrogen (N_2).

Because we were concerned with the spectral region of the *casi* from 0.4 to 0.9 μm, we were only interested in path radiance and gaseous absorbers in the VNIR region. In this region O_2 has three absorption bands centered at 0.63, 0.69, and 0.76 μm; O_3 exhibits absorption from 0.45 to 0.77 μm; and H_2O has absorption features centered at 0.72, 0.82, and 0.94 μm.

The ATmospheric REMoval program (ATREM) (CSES, 1997; Gao *et al.*, 1993) was used for the atmospheric modeling and surface reflectance retrieval of the spectral mode data. ATREM requires information about the time and place of the image acquisition (Table 1), atmospheric conditions during the image acquisition (Table 1), and a wavelength file of the spectral configuration including center wavelengths and FWHMs (see Spectral Calibration: Preliminary Apparent Surface Reflectance).

ATREM estimates water vapor from a three-channel ratioing technique based on the water absorption features in the 0.94- and 1.14-μm regions (CSES, 1997; Gao *et al.*, 1993). These features are not present in the spectral range of the *casi*. The *casi* exhibits two small water absorption bands centered at 0.722 μm and 0.822 μm. The 0.722-μm feature is on the red edge of the vegetation spectrum and does not have a distinct feature for water vapor retrieval. The 0.822-μm feature was used as the only input. This was a reasonable approach, which has previously been used successfully.

ATREM was developed with an emphasis on AVIRIS, which has a 10-nm resolution and a flying altitude of 20 km. Platform altitude is important for the effect of path radiance, and changes in spectral resolution affect the shape of the absorption features (Goetz and Heidebrecht, 1996). ATREM has been modified to handle varying sensor altitudes but not higher resolution data. This study shows, however, that ATREM may be applied to low flying airborne sensors at resolutions greater than 10 nm (see Radiometric Calibration: Path Radiance and Transmittance, Figures 4 and 5).

MODTRAN (Berk *et al.*, 1989) was used to model a path radiance profile to assess the quality of the radiometric calibration. An atmospheric profile, an aerosol profile, and the visibility at the time of the data acquisition are the key parameters. MODTRAN uses a band model to model the absorption and scattering of radiation through the atmosphere. Both Rayleigh and Mie scattering are modeled as well as the interaction between molecular scattering and absorption.

Oxygen-Fitting Algorithm

The oxygen-fitting algorithm (Goetz *et al.*, 1995; Goetz and Heidebrecht, 1996) takes advantage of the changing shape of the narrow oxygen absorption feature centered around 0.762 μm. Oxygen transmittance curves were computed for 100 different sets of band centers that varied by 0.1 nm. The ratio of the slopes of the two sides of the oxygen feature was calculated for each set of band centers. These ratios were compared to the ratio of the sides of the oxygen feature of each continuum-removed image spectrum to find the corresponding band center. The result is an "oxygen band center" image.

Radiometric Calibration

Three aspects of radiometric calibration were examined: the relative effect of path radiance on the measured signal was modeled, absorption features for different gases in the atmosphere were modeled and interpreted in relation to a radiance profile, and the minimum radiance value recorded in each band was compared to a path radiance profile.

Path Radiance and Transmittance

The radiance profile from the spectral mode image data shows the spectral characteristics of a vegetated surface (Figure 3). The green reflectance peak around band 30, the chlorophyll absorption in the region around band 54, and the red edge in the near IR are distinct. The additive path radiance component is not distinctly exhibited in this radiance profile.

Many absorption features are exhibited in the radiance profile. Oxygen absorption is visible at band 70, and absorption by water vapor is visible at bands 62, 81, and 93 to 96. The absorption from ozone is not directly distinguishable. Modeling of transmittance using ATREM (Figure 4) showed that predicted absorption features of water vapor and oxygen are consistent with the absorption features in the radiance profile.

Using ATREM, the effect of path radiance on apparent surface reflectance under different aerosol loads was modeled (Figure 5). This showed that, at a sensor altitude of 1500 m, even under an extreme aerosol load of 5 km visibility, the scattered light contribution is at most 5 percent. This may explain the decrease in radiance at wavelengths shorter than 0.55 μm

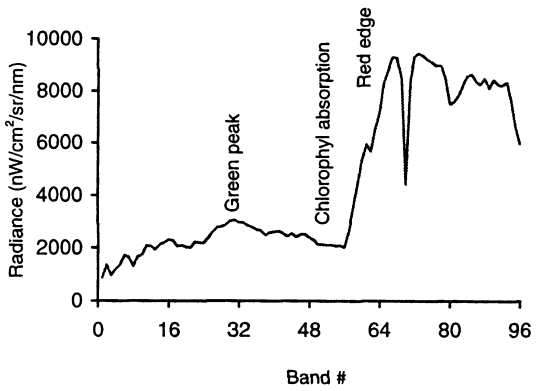

Figure 3. Radiance profile from the spectral data. The green peak, the chlorophyll absorption, and the red edge are clearly visible, as are several atmospheric absorption features.

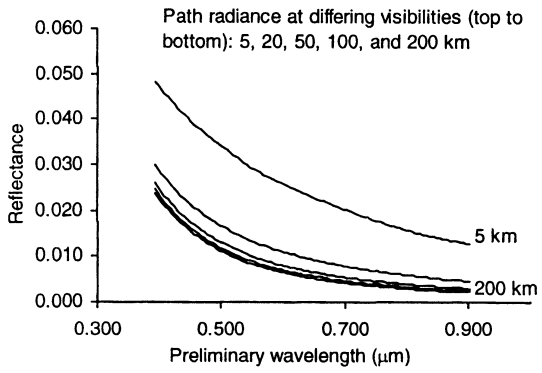

Figure 5. Effect of different aerosol loads on apparent surface reflectance. Even under extremely turbid atmospheric conditions (visibility 5 km), atmospheric reflectance at a target with surface reflectance zero is at most 5 percent.

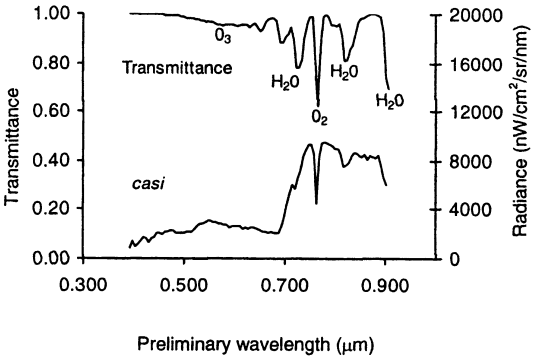

Figure 4. Transmittance during image acquisition. The absorption features from water vapor, ozone, and oxygen are clearly visible and comparable to the absorption features on the image spectrum.

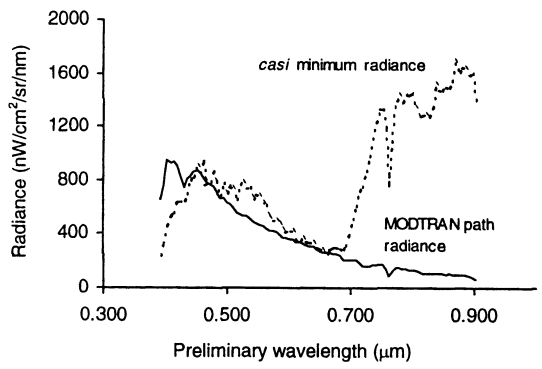

Figure 6. Path radiance spectrum and minimum radiance spectrum in spectral mode. Path radiance exceeds minimum recorded radiance in the shorter wavelengths and around the chlorophyll absorption feature (barely visible in the figure).

(the green peak) seen in Figures 3 and 4 and the difference between the AVIRIS and the *casi* radiance seen in Figure 2.

The radiometric calibration of the detectors was evaluated using a path radiance spectrum from MODTRAN assuming zero surface reflectance. Readings from two meteorological stations within a radius of 10 and 35 km from the investigation area indicated a visibility between 30 and 35 km (Danish Meteorological Institute/Weather and Climate Information Division). The MODTRAN spectrum was modeled with 35 km visibility and compared to a spectrum of the minimum radiance detected in each band. The minimum radiance was calculated on a subset of the image from pixel 16 to restrict the spectral calibration accuracy to < 0.25 nm (see Spectral Calibration: Oxygen Absorption). Path radiance exceeded the minimum radiance recorded in bands 1 to 56 (up to 0.687 μm). The majority of the pixels with low radiance values were recorded in column 39, which visually appeared a little darker than the other columns; therefore, column 39 was excluded. The resulting minimum *casi* radiance from columns 16 to 38 and path radiance is shown in Figure 6.

The minimum image radiance exceeds the modeled path radiance at the green peak around 0.55 μm and also from the red edge into the near IR region. The investigation area was a gently undulating moraine landscape covered by vegetation. No dark shadows were present and the shade from vegetation was so light that irradiance still reached the surface and the spectral characteristics of vegetated surfaces were visible. Below 0.448 μm the recorded brightness starts to drop off significantly relative to the modeled path radiance. The path radiance is seen to exceed recorded minimum *casi* radiances in several bands up to 0.467 μm and around 0.662 μm.

For a surface reflectance of zero, an airborne or spaceborne scanner will measure only path radiance. The minimum signal in any band should equal at least the path radiance. The drop-

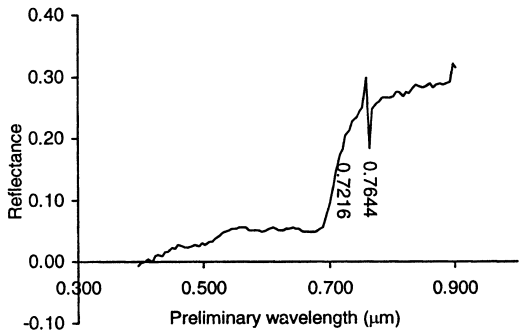

Figure 7. Apparent surface reflectance using preliminary wavelength file. A spectral shift in the oxygen absorption is clearly seen in the data. The water vapor feature on the red edge and the left side of the water vapor absorption feature at 0.94 μm has not been removed. Negative reflectance occurs in the shortest wavelengths.

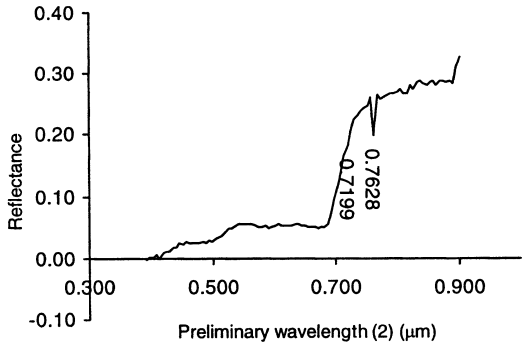

Figure 8. Apparent surface reflectance after applying a constant shift to the preliminary band center positions, creating a new wavelength file called preliminary wavelengths (2). The shift in the oxygen absorption feature is removed with a new band center positioning at 0.7628 μm. The water vapor features around 0.722 μm at 0.7199 μm were also nicely removed. An increase in the longest wavelength and the negative reflectance in the shorter wavelengths are still seen.

off in the *casi* data could be due to bad data points, but image statistics showed that this was not the case. Several percent of the data had a lower signal than the path radiance in the spectral region below 0.467 μm. Thus, the radiometric calibration is regarded to be insufficient in the shorter wavelengths. Many bumps and wiggles are seen in the minimum radiance profile up to around 0.524 μm, and possibly the poor calibration extends further into the spectral range. The drop-off around 0.662 μm was considered to be caused by low reflectance levels around the chlorophyll absorption feature. The number of affected pixels was small, and these were located in the shade of the forested areas with little or no direct incident light. The visibility in the modeling was set to the highest possible level, and there was no reason to believe that the path radiance was overestimated compared to the actual conditions during the image acquisition.

In the spatial data set the poor radiometric calibration in the shorter wavelengths affected the first two bands at center wavelengths 0.424 and 0.475 μm, an indication that the poor radiometric calibration stretches beyond 0.467 μm. However, only a few points that were affected in band 2. The low reflectance effect was seen in bands 5, 6, and 7 at center wavelengths 0.601, 0.650, and 0.682 μm, but less than 20 pixels were recorded with a minimum radiance below path radiance at the given atmospheric conditions.

Spectral Calibration

The quality of the spectral calibration was also assessed from the spectral mode data because, again, a continuous spectrum was required. The approaches were retrieval of apparent surface reflectance and determination of the location of the center wavelength of the oxygen absorption feature.

Preliminary Apparent Surface Reflectance

Apparent surface reflectance (Figure 7) was retrieved using ATREM with preliminary band centers estimated by dividing the spectral range of 392.6 to 906.2 nm into 96 equal intervals of 5.4 nm. The FWHM was estimated to be 6.6 nm as opposed to the *casi* specification of 2.2 nm FWHM and 1.8 nm sampling.

The most dominant feature in the derived spectral reflectance is a distinct spectral shift in the oxygen absorption feature (0.7644-μm preliminary center wavelength) which occurs when the position of the center wavelengths is inaccurate (Goetz *et al.*, 1995). Because of the problems with the position of the center wavelengths, the water vapor band at 0.722 μm (0.7216-μm preliminary center wavelength) was not completely removed. The shape of the spectrum made it more difficult to evaluate the water vapor removal at 0.822 μm. The sharp increase at the end of the spectrum may be the result of a spectral shift of the 0.94-μm water vapor feature or an overcompensation for the water vapor absorption. The poor radiometric calibration discussed earlier, combined with a possible ATREM overestimation of the scattering component, caused reflectance below zero in the short wavelengths.

New band centers were derived to remove the spectral shift in the oxygen absorption feature. The best band center for the oxygen feature was found by shifting the wavelengths by 0.1 nm until the best fit occurred. The best fit across the image was at approximately 762.8 nm (Figure 8) but no discrete wavelength could be found. Every individual detector, or possibly even every individual pixel, needed its own wavelength calibration, a problem that may occur using a linear array scanner (Goetz and Heidebrecht, 1996). A shift of 1.6 nm was subtracted from the original band centers to generate a new set of band centers called "preliminary center wavelength (2)."

Figure 8 shows that the repositioning of the oxygen absorption band center removes the spectral shift, but the removal of the atmospheric oxygen absorption feature is still incomplete. Spectral atmospheric transmission values in ATREM are based on HITRAN (Rothman *et al.*, 1987) and resampled to provide an equal wavelength spacing of 2.5 nm and 10 nm resolution. The wavelength spacing in *casi* was 5.4 nm and in the FWHM was 5.8 nm (see Note). The shape of the O_2 band is dependent not only on the spectral calibration and wavelength spacing but also on the shape of the reflectance curve (Goetz *et al.*, 1995). The incomplete removal may therefore be caused by difficulties in atmospheric modeling rather than poor spectral calibration. Figure 4 shows that ATREM models the oxygen feature, and constraints on atmospheric modeling are less likely. Figure 8 also shows that the water vapor at 0.722 μm is now well removed. There was no improvement in the negative reflectance at the

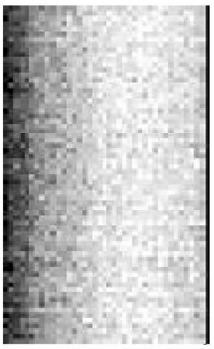

Figure 9. Sub-image of the derived oxygen absorption band center positions. The grey scale of the pixels indicates absolute deviation in nm of the oxygen absorption band center positions from 0.7628 μm. Darkest pixels equal largest deviation (see Figure 10 for comparison). The very dark line to the right is the ILS signal.

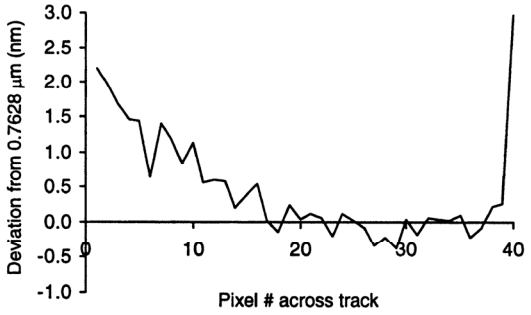

Figure 10. Across-track profile of the oxygen image. Deviation in nm from 0.7628 μm. The spectral calibration precision clearly decreases towards the left part of the scanner, and positive deviations up to 2 nm were found. The very high value in pixel 40 is the ILS signal.

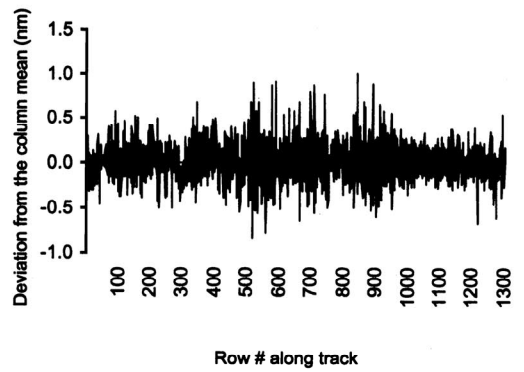

Figure 11. Along-track profile of the oxygen image. Deviation in nm from the mean oxygen position of the column.

shortest wavelengths, and the increase in reflectance at the very long wavelengths also occurred after shifting the center wavelengths.

Oxygen Absorption

The precision of the spectral calibration was assessed using an oxygen fitting algorithm (Goetz *et al.*, 1995) to locate the center position of the 0.762-μm oxygen absorption feature in every pixel. A subset of the image of the position of the oxygen absorption feature (Figure 9), a horizontal profile across the image (Figure 10), and an along-track profile of the oxygen image (Figure 11) show that the position of the oxygen feature is not constant throughout the image and that there was a problem with the spectral calibration precision.

Furthermore, Figures 9 and 10 show that there was a problem with spectral alignment across the scanner. The problem was definitely greatest in relation to the 5° discrepancy in the left-most part of the scanner as reported by the operating company. A 42° FOV covering 512 pixels indicates that at 5° a pixel spacing of eight should affect six pixels. The standard deviation in nanometers from the mean position of the oxygen absorption feature along track showed that the spectral calibration precision for the detectors in the spectral image was between $\pm$0.31 and $\pm$0.19 nm depending on the position across track (Figure 10). The largest standard deviations were found in the left part of the detector matching the reported information about the discrepancy.

It was however evident from Figures 9 and 10 that the scanner discrepancy stretched much further across than six pixels. The skewness of the probability density function (PDF) (Figure 12) of the whole oxygen image was -1.33. Fifteen pixels with a pixel spacing of eight pixels had to be removed from the subsetted image to obtain a standard deviation of less than $\pm$0.25 nm, equaling the mean of the along-track calibration precision (Figure 11). This changed the PDF to a histogram of a reasonable Gaussian distribution (Figure 13) with a skewness of -0.33. The kurtosis changed from 1.24 to 1.06.

It is concluded that, at a 5.4-nm sampling interval, the accuracy of the spectral calibration must be better than 0.25 nm in order to account for the sharp oxygen absorption feature at 0.762 μm. Generally, the necessary precision depends on the shape of the absorption features. For example, in the water vapor absorption region from 0.7 to 2.3 μm, an accuracy of 0.1 nm was found to be desirable at a 10-nm sampling interval (Goetz *et al.*, 1991).

Surface Reflectance Retrieval

Surface reflectance was retrieved for both the spectral and spatial image data. The methodology was determined by the data available for the project. In our study we acquired field measurements for one calibration target (a gravel parking lot) and we used a combination of modeling and empirical approaches for the reflectance retrievals.

Spectral Data

The spectral-mode image data allowed for correction of water vapor absorption on a pixel-by-pixel basis; thus, ATREM was used to derive surface reflectance. Thirty field spectra measured with the GER2100 field spectrometer and four *casi* image spectra were retrieved over a calibration site (Figure 14). The calibration site was a gravel parking lot visible as a rectangular area in the subset images in Figure 1.

The shape is generally the same for the field and image gravel spectra. The decrease below 0.5 μm in the derived spectrum is due to the poor radiometric calibration discussed ear-

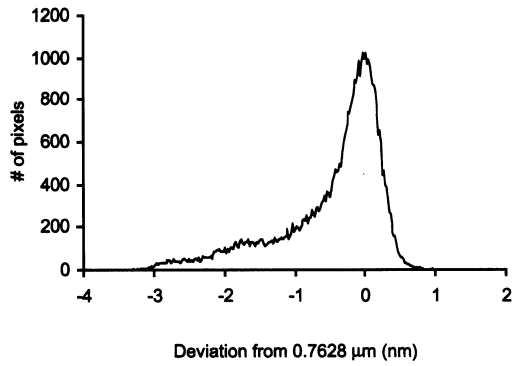

Figure 12. Histogram (PDF) of the oxygen image before subset. The poorly calibrated pixels at the left side cause skewness towards the left.

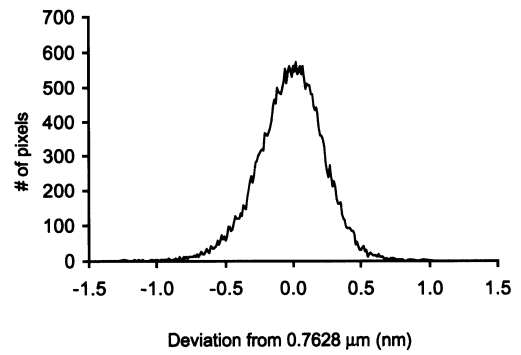

Figure 13. Histogram (PDF) of the oxygen image after subset. The histogram approaches a normal distribution function.

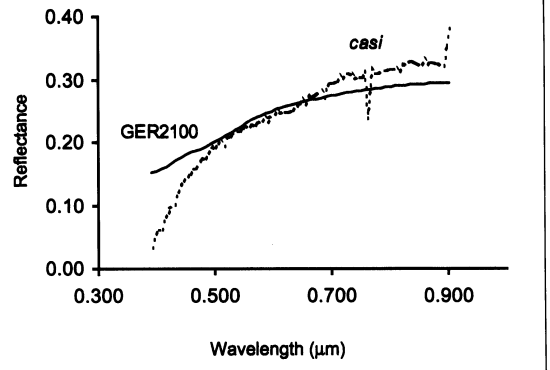

Figure 14. Field measured (solid) and retrieved image (dotted) gravel spectra. Retrieved spectrum is lower than the field spectrum below 0.5 μm, coherent between 0.5 and 0.7 μm, and higher beyond 0.7 μm. The field spectrum is the average of 30 spectra, and the image spectrum is an average of four pixels. The field spectra were measured during the overflight.

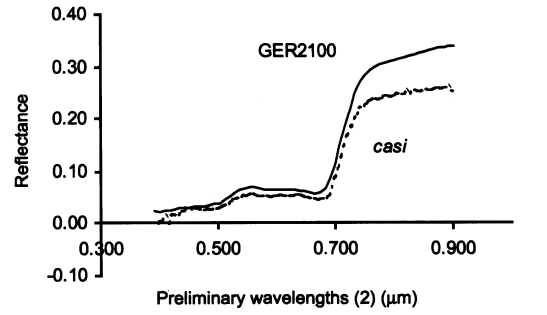

Figure 15. Derived normalized vegetation reflectance spectrum (dotted) and field measured spectrum (solid). The two spectra show good resemblance. The difference in magnitude in the NIR is evident because the image pixel and field measurement locations were not identical.

lier and an overestimation of the scattering component by ATREM. On the whole, image negative reflectance was present up to 0.489 μm, which implies that the poor radiometric calibration may stretch beyond 0.467 μm as suggested. Figure 6 showed that the MODTRAN simulation of path radiance exceeded minimum recorded *casi* radiance around 0.662 μm and, as a result, a few pixels had negative reflectance in this wavelength region. In Figure 14 there is no negative reflectance around 0.662 μm because the parking lot returns a relatively high signal to the scanner at short wavelengths and around the chlorophyll absorption feature. The retrieved reflectance beyond 0.7 μm is a little higher in the derived spectrum, the incomplete removal of the oxygen feature is seen, and the sharp increase from the 0.94-μm water vapor feature is also visible.

Because the oxygen feature was not completely removed and ATREM tends to overestimate the atmospheric scattering, spectral reflectance was normalized to the calibration target using the data in Figure 14 (see, e.g., Clark *et al.* (1995)). An image vegetation spectrum after normalization and a field vegetation spectrum are shown in Figure 15. The normalization removed the residual oxygen and water vapor features and the spectrum shows good resemblance to the field spectrum. The field spectrum was arbitrarily chosen from the time of the overflight and was not identically matched to a pixel in the image. Accordingly, a shift in magnitude is seen between the two spectra.

Spatial Data

The non-continuous spectral configuration in the spatial data does not allow for water vapor absorption correction on a pixel-by-pixel basis. Apparent surface reflectance was retrieved using a modified empirical line calibration. The offset in the calibration was obtained from the MODTRAN path radiance spectrum (Figure 6) resampled to the spectral configuration of the spatial mode. The multiplicative factors were

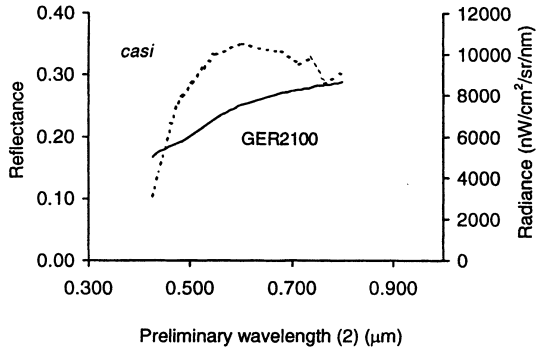

Figure 16. Field measured (solid) and radiance image gravel spectra from the spatial mode image. The water vapor absorption and the oxygen absorption are seen in bands 8 (0.715 μm) and 10 (0.769 μm), respectively.

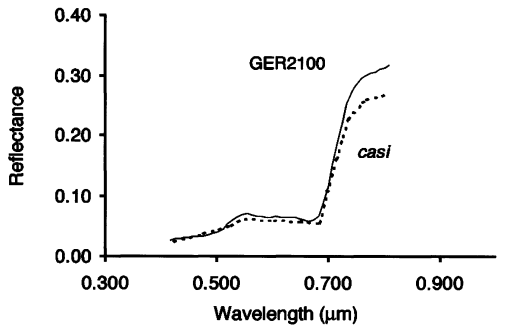

Figure 17. Derived vegetation reflectance spectrum (dotted) and field measured spectrum (solid) from the spatial mode image. There is a good resemblance between the two spectra. Again, there is a difference in magnitude in the near IR because the image pixel and field measurement location were not identical.

obtained from ratioing the ground calibration site and the image radiance spectrum (Figure 16). Again, 30 field spectra were averaged, but this time the full spatial coverage of the spatial mode data allowed for an average of 37 image spectra.

The oxygen absorption in band 10 (0.769 μm) and water vapor absorption in band 8 (0.715 μm) are visible in a radiance spectrum from the spatial data. Negative reflectance in the spatial reflectance image is seen in bands 1, 2, 5, 6, and 7 (centered at 0.424, 0.475, 0.601, 0.650, and 0.682 μm) as a direct result of subtracting the MODTRAN path radiance previously discussed.

Figure 17 shows a derived vegetation spectrum and a field vegetation spectrum measured with the GER2100. Again, the field spectrum was not identically matched to an image pixel.

Overall, the resemblance to a field spectrum is good. The oxygen absorption feature in band 10 (centered at 0.769 μm) and the water vapor feature in band 8 (centered at 0.715 μm) have been removed. The oxygen feature was removed in every pixel in a subset image excluding the columns most affected by the discrepancy in the left part of the scanner. The problem with spectral precision did not impact the ability to remove atmospheric features from these non-continuous spectra with approximately 10 nm FWHM. The request for spectral calibration accuracy decreased with decreasing spectral resolution (broader bands).

Conclusion/Summary

This paper describes methods for assessing the radiometric and spectral quality of hyperspectral *casi* images when little or no radiometric or spectral information was available.

Radiometric calibration was evaluated using atmospheric modeling. A path radiance profile was compared to the minimum radiance recorded in each band. The minimum image radiance was influenced by the dominating vegetated signal. Minimum radiance was lower than path radiance below 0.467 μm and around 0.662 μm in the spectral mode, and it was concluded that the radiometric calibration was poor at shorter wavelengths and at low signal levels around the chlorophyll absorption feature. One detector (column 39) was particularly poorly calibrated. Because of the spectral configuration, the poor radiometric calibration influenced bands 1 and 2 and bands 5, 6, and 7 in spatial mode. The quality of the radiometric calibration was assessed from data with a spectral calibration precision within $\pm$0.25 nm.

We used atmospheric modeling and an oxygen-fitting algorithm to assess the wavelength calibration. We calculated a preliminary wavelength file by dividing the whole spectral range of the scanner from 396.2 nm to 902.6 nm into 96 bands of bandwidth 5.4 nm. Atmospheric modeling of apparent surface reflectance revealed a spectral shift around the oxygen feature. Shifting the center wavelengths by 1.6 nm removed the shift and we found that the strongest oxygen absorption feature in band 70 was located at 762.8 nm. The match was not perfect in every pixel, and it was concluded that a spectral accuracy should be better than 0.25 nm at a 5.4-nm sampling interval in order to handle the sharp absorption feature from oxygen and that every pixel may need its own spectral calibration in a linear array scanner.

Spectral calibration precision was evaluated from an image of the location of the oxygen feature. The spectral precision along track was $\pm$0.25 nm, whereas the spectral precision across track varied from $\pm$0.19 nm to $\pm$0.31 nm. The along-track standard deviation of $\pm$0.25nm was exceeded by the 15 left-most pixels of the scanner, and it could be concluded that the discrepancy was more than the 5° reported by the operating company.

Apparent surface reflectance was retrieved with different methods for the spectral and spatial modes. Water vapor absorption was removed on a pixel-by-pixel basis in the spectral image. The residuals from oxygen absorption and other artifacts were removed by normalizing to a calibration site. Negative reflectance was present at shorter wavelengths and around the chlorophyll absorption feature due to the radiometric calibration and a possible overestimation of the scattering component by ATREM. The general shape of an image vegetation spectrum matched a field vegetation spectrum well. The spatial mode data were calibrated to apparent surface reflectance by subtracting a modeled path radiance profile and applying gain factors from the calibration site. Again, the general shape of an image vegetation spectrum matched a field vegetation spectrum well. Negative reflectance was found in bands 1, 2, 5, 6, and 7.

The methods used performed well and fulfilled the purpose of the study. Examples of applications of *casi* data in the literature show that emphasis is often placed on the spatial data set. Assessing the quality of the radiometric and spectral calibration of the scanner requires a continuous spectrum, and it is

recommended that spectral mode data be acquired simultaneously with spatial mode data in a *casi* campaign.

Note

Eight months after the data acquisition, the operating company supplied us with an update on the spectral calibration. The spectral range of the 96 bands using row summation factor three was 394.3 to 904.3 nm and the FWHM was 5.8 nm. The position of the oxygen feature at 762.8 nm was confirmed. The spectral configuration of the spatial mode was confirmed as the one specified and listed in Table 2.

Acknowledgments

The authors would like to acknowledge the Danish Space Board for funding the DANish Multisensor Airborne Campaign, ITRES Research Limited, the manufacturer of *casi*, for support for image data acquired with a *casi* scanner outside of their reach of maintenance, and the Danish Meteorological Institute/Weather and Climate Information Division for information on weather conditions.

The analyses of the data were performed during an exchange program with the Center for the Study of Earth from Space (CSES), CIRES, University of Colorado. The first author would like to thank the Director and the administrative and scientific staff at CSES for scientific discussions, support, and encouragement.

References

Baulies, X., and X. Pons, 1995. Approach to forestry inventory and mapping by means of multi-spectral airborne data, *Int. J. Remote Sensing*, 16(1):61–80.

Berk, A., L.S. Bernstein, and C.C. Robertson, 1989. *MODTRAN: A Moderate Resolution Model for LOWTRAN 7*, Final Report, GL-TR-0122, AFGL, Hanscom AFB, Massachusetts, 42 p.

Center for the Study of Earth from Space (CSES), 1997. *Atmospheric REMoval Program (ATREM), User's Guide, Version 3.0*, Cooperative Institute for Research in Environmental Sciences (CIRES), University of Colorado, Boulder, 27 p.

Clark, R.N., G.A. Swayze, K.B. Heidebrecht, R.O. Green, and A.F.H. Goetz, 1995. Calibration to surface reflectance of terrestrial imaging spectrometry data: Comparison of methods, *Summaries of the Fifth Annual JPL Airborne Earth Science Workshop*, Jet Propulsion Laboratory, Pasadena, California, 1:41–42.

Gao, B., K.B. Heidebrecht, and A.F.H. Goetz, 1993. Derivation of Scaled Surface Reflectances from AVIRIS data, *Remote Sens. Environ.* 44:165–178.

Goetz, A.F.H., C.O. Davis, J.D. Aber, K.L. Carder, R.N. Clark, J. Dozier, S.A.W. Gertsl, H. Kieffer, D.A. Landgrebe, J.M. Melack, L.C. Rowan, S.L. Ustin, R.M. Welch, and C.A. Wessman, 1991. *High Resolution Imaging Spectrometer (HIRIS) Science Requirements*, HIRIS Science Requirements Document, JPL Report D-7843, Jet Propulsion Laboratory, Pasadena, California, 25 p.

Goetz, A.F.H., K.B. Heidebrecht, and T.G. Chrien, 1995. High accuracy in in-flight wavelength calibration of imaging spectrometry data, *Summaries of the Fifth Annual JPL Airborne Earth Science Workshop*, Jet Propulsion Laboratory, Pasadena, California, 1:67–69.

Goetz, A.F.H., and K.B. Heidebrecht, 1996. Full-scene, subnanometer HYDICE wavelength calibration, *Proceedings of SPIE*, 2821:85–92.

Iqbal, M., 1983. *An Introduction to Solar Radiation*, Academic Press, Toronto, Canada, 390 p.

Jacobsen, A., N.H. Broge, and B.U. Hansen, 1995. Monitoring wheat fields and grasslands using spectral reflectance data, *Proceedings of the First International Symposium on Spectral Sensing Research*, 26 November–01 December, Melbourne, Australia (available on CD-rom from Commonwealth Information Services, Australian Government Publishing Service, GPO Box 84, Canberra, ACT 2601, Australia. ISBN No. 0 644 35625).

Rothman, L.S., R.R. Gamache, A. Goldman, L.R. Brown, R.A. Toth, H.M. Pickett, R.L. Poynter, J.-M. Flaud, C. Camy-Peyret, A. Barbe, N. Husson, C.P. Rinsland, and M.A.H. Smith, 1987. The Hitran Database: 1986 Edition, *Appl. Opt.*, 26(19):4058–4097.

Vane, G., R.O. Green, T.G. Chrien, H.T. Enmark, E.G. Hansen, and W.M. Porter, 1993. The Airborne Visible/Infrared Imaging Spectrometer, *Remote Sens. Environ.*, 44:127–143.

(Received 19 January 1999; accepted 12 August 1999; revised 08 November 1999)